

RESEARCH

Open Access



# Experimental Study on Damage Evaluation, Pore Structure and Impact Tensile Behavior of 10-Year-Old Concrete Cores After Exposure to High Temperatures

Xudong Chen<sup>1,2\*</sup> , Dandan Shi<sup>2</sup> and Shengshan Guo<sup>3</sup>

## Abstract

High temperatures impose a negative effect on the mechanical properties of concrete. An experimental setup designed by the theory of nonlinear resonance vibration, the method of mercury intrusion porosimetry (MIP) and split Hopkinson pressure bar (SHPB) were used to test damage, porosity and mechanical properties of the pre-heated Brazilian discs of 10-year-old concrete respectively. According to the nondestructive test, the hysteretic nonlinearity parameters  $\beta_n$  became larger as the temperature went up. The damage calculated by  $\beta_n$ , which was 0, 0.57, 0.88 and 0.95 at 20 °C, 200 °C, 400 °C and 600 °C respectively, could be fitted by a power function. Based on MIP, the compound lognormal distribution model was used to simulate the pore size distributions. The quantitative relationship between porosity and damage was established by a power function, with the porosities of 13.96% at 20 °C, 15.77% at 200 °C, 19.17% at 400 °C and 20.22% at 600 °C. Finally, by the method of impact splitting tensile tests under gas pressures of 0.3 MPa, 0.4 MPa and 0.5 MPa, which represented impact velocity of 7.11 m/s, 10.26 m/s and 13.02 m/s respectively, the dynamic tensile strengths were obtained and the quantitative relationship between damage and macroscopic splitting tensile strength was established and the average value of exponential parameter  $b$  was 0.281.

**Keywords:** 10-year-old concrete cores, high temperatures, nonlinear resonance vibration, mercury intrusion, splitting

## 1 Introduction

Fire often occurs in concrete structures when they are in service and the mechanical properties of concrete decrease obviously after exposure to high temperatures, although the material appears a good performance of resistance to fire and heat (Bažant and Kaplan 1996; Gao et al. 2017; Eunmi et al. 2018). During the process of fire, the magnitude of temperature and the duration of the fire can cause different degrees of damage to concrete structures. Such conditions may result in cement paste

matrix shrinkage, and the spalling of concrete may occur especially when the moisture content of concrete is high (Park and Yim 2017; Choi et al. 2017). The degree of damage, which is directly related to the mechanical behavior of concrete, is very important for the evaluation of concrete structure safety. If the concrete structures are still put into use when the damage is not measured and evaluated properly, failures often occur because the residual strength cannot withstand the constant load and the incidental load. As a result, it is of a great significance about how to detect concrete damage quickly and accurately.

When concrete is subjected to high temperatures, the aggregation of microscopic defects, which is mainly presented by the variation of pore radius and porosity (Güneyisi et al. 2008; Pei et al. 2017), is a main reason for the accumulation of damage. In the past 30 years, as the

\*Correspondence: cxdong1985@hotmail.com

<sup>1</sup> Key Laboratory of Concrete and Prestressed Concrete Structures of the Ministry of Education, School of Civil Engineering, Southeast University, Nanjing 210096, China

Full list of author information is available at the end of the article  
Journal information: ISSN 1976-0485 / eISSN 2234-1315

study of macroscopic mechanical properties of concrete gradually became mature, the research on microscopic behaviors of concrete has been the hotspot in the research field (Ji et al. 1997; Chen et al. 2013). Besides, studies have shown that the engineering properties of concrete such as strength (De Bruyn et al. 2017; Hager et al. 2016), permeability (Zhang and Li 2011) and durability (Gonzalez-Corominas et al. 2016) are highly dependent on pore structures. The mercury intrusion porosimetry (MIP), which is widely applied to the study of the pore structures of concrete materials, is a vital means of analyzing the microstructure of concrete and is well-received in the research field of concrete. Zhang (1998) studied the variation of the porosity of concrete by means of MIP, helium flow and nitrogen adsorption after the concrete specimens were subjected to four-point flexural tensile fatigue tests. Chan et al. (2000) studied the variation of porosity and pore structure by utilizing MIP and established the quantitative relationship between porosity and compressive strength of concrete after the concrete was exposed to high temperatures. Chen et al. (2015) performed a dynamic compression test of plain concrete based on the split Hopkinson pressure bar, and established a relationship between the dynamic compressive strength and the porosity obtained by MIP. Because of the convenience, the applicability and the accuracy of mercury intrusion, the research method has been widely received by researchers.

Although there are several methods of measuring the damage of concrete in the field of nondestructive examination, it is still hard to recognize which method is the most accurate for the measurement (Zhang et al. 2017). The techniques for evaluating the fire-damaged concrete are mainly divided into three categories (Park et al. 2014): overall inspection (ultrasonic pulse velocity, ultra pulse-echo and impact echo), surface evaluation (Schmidt rebound hammer, Windsor probe and spectral analysis of surface waves) and special point evaluation (small-scale mechanical testing, scanning microscopy and thermoluminescence analysis). Some techniques of nondestructive examination, e.g. ultrasonic pulse velocity, cannot accurately detect contact-type defects, although they are suitable for in situ tests. Some other techniques such as scanning microscopy and thermoluminescence analysis demand good laboratory equipment and are quite time-consuming. In recent years, Abeele et al. (2000) have proposed a nonlinear resonance vibration method, which greatly overcomes the shortcomings of various measurement methods mentioned above. The nonlinear resonance vibration method describes the hysteretic nonlinearity by means of the phenomenological model. Based upon the phenomenological model, the constitutive relationship between the stress and the elastic modulus can be shown as follows:

$$\sigma = \int M(\varepsilon, \dot{\varepsilon}) d\varepsilon \quad (1)$$

$$M(\varepsilon, \dot{\varepsilon}) = M_0 \left\{ 1 - \beta\varepsilon - \delta\varepsilon^2 - \alpha[\Delta\varepsilon + \varepsilon(t)\text{sign}(\dot{\varepsilon})] + \dots \right\} \quad (2)$$

where the parameters  $\beta$  and  $\delta$  are the classical nonlinear perturbation coefficients,  $\alpha$  is the nonlinear hysteretic coefficient,  $\varepsilon$  is the strain,  $\sigma$  is the stress,  $\dot{\varepsilon}$  is the strain rate,  $\Delta\varepsilon$  is the local strain amplitude in the previous period,  $M_0$  is the linear modulus and  $\text{sign}(\dot{\varepsilon}) = 1$  if  $\dot{\varepsilon} > 0$  or  $\text{sign}(\dot{\varepsilon}) = -1$  if  $\dot{\varepsilon} < 0$ . Studies have shown that amplitude-dependent resonance characteristics, which can be used to characterize damage, such as nonlinear attenuation, harmonic generation and amplitude-dependent resonance frequency shift, are highly sensitive to contact-type defects distributed in different materials (Abeele et al. 2001; Park et al. 2015).

Strength, which is highly sensitive to strain rates, is the most important property of concrete materials. In realistic condition, some concrete structures like nuclear power station and chemical plant are often subjected to impact and explosive loadings. At high loading rates, concrete shows quite different behavior to that of quasi-static condition, and the researches in the dynamic research field are still not sufficient. According to fracture mechanics, cracks caused by tension can result in stress concentration, and then reduce the overall loading capacity. However, because of the usage of reinforced steel bars in engineering construction, the tensile strength of concrete has not been paid enough attention and the corresponding research achievements are comparatively hard to see. As a result, it is necessary to conduct studies of dynamic tensile strength of concrete. Feng et al. (2018) studied the energy absorption capabilities of rubber concrete by conducting dynamic splitting tensile tests, and compared the rate sensitivity of rubber concrete to that of plain concrete. Zhang et al. (2006) conducted experimental studies on splitting tensile properties of 74 mm-diameter concrete specimens and studied the mechanism and speed of crack propagation of concrete specimens.

Macroscopic mechanical properties of concrete are highly influenced by its microscopic conditions. When the porosity of concrete increases, the damage increases while the external strength decreases. For a further comprehension of concrete damage mechanism, some researchers conducted both microscopic and macroscopic tests to perform a quantitative study on the relationship between them. Parra et al. (2011) conducted a splitting tensile test on self-compacting concrete of different ages and analyzed the porosity at the same time. The results show that the addition of limestone fines creates lower porosity with lower splitting strength than normally-vibrated concrete.

Kumar and Bhattacharjee (2003a) obtained the pore size distribution and porosity of concrete by MIP and established an empirical model relating the in situ strength of concrete with porosity, pore size distribution and several materials properties. For the study of concrete damage, it is often considered only when concrete is affected by environmental conditions (high temperatures, freeze–thaw cycles) or external loads. Isojeh et al. (2017) studied the damage of concrete caused by fatigue loading and proposed a quasi-empirical model of damage and concrete residual strength. Monette et al. (2002) made concrete damage by alkali-silica reaction and studied the relationship between damage and residual strength. Researches on the relationship between pore structures and damage, and that between damage and tensile strength at ambient temperatures can be found, but the relationship of the three can hardly be studied simultaneously, especially after concrete is exposed to high temperatures. Thus, there is a need to study the relationship between concrete damage, porosity and tensile strength.

In the study, nonlinear resonance vibration tests, mercury intrusion porosimetry tests and splitting Hopkinson pressure bar tests were conducted in order. To make the framework of the research more clearly, the testing procedure of the above three tests were introduced first. Then the testing results were analyzed and divided into different sections, and these sections were linked by damage index, pore structures and dynamic splitting strength obtained in different tests. Discussion is also presented to show the insufficiency of the work and the outlook for further study. Finally, the conclusion is drawn.

## 2 Experimental Program

### 2.1 Specimen Preparation

The concrete mix proportions in the test are shown in Table 1. The specimen geometry of Brazilian disc with a diameter of 74 mm and a length of 37 mm, was adopted. The concrete was a mixture of ordinary Portland cement and secondary fly ash, river sand with particle size distribution fitting ASTM C33 (2004), aggregates of 20 mm maximum size, portable water and polycarboxylate water reducer to obtain a good flow-ability. In order to simulate the realistic service condition of concrete materials in structures, concrete beams of dimensions 300 mm × 300 mm × 500 mm were cast by using the designed mix 10 years ago. A wet cloth was used to cover the casted beams and was kept wet by sprinkling water

for adequate curing of concrete beams in the 1st month. By drilling perpendicular to the casting direction of the concrete beams, the cores were then cut as a diameter of 74 mm 10 years after the concrete was casted. The old concrete specimens were cut in height of 37 mm before the test was performed, controlling the aspect ratio as 1:2. It should be noted that concrete used in the study can only be used for the evaluation of 10-year-old concrete structures, because the property of concrete varies largely with ages. For structures made of fresh concrete or older concrete, corresponding researches should be made in the further study. The compressive strength and the Young's modulus of the 10 years old concrete were 79.4 MPa and 42.1 GPa, respectively.

Before the damage evaluation, the old concrete cores were put into a heating furnace for high temperature pre-heating. The temperatures variables in the test were 20 °C (normal temperature), 200 °C, 400 °C and 600 °C. Eleven specimens were heated on the condition of the temperatures mentioned above. A constant furnace heating rate of 10 °C/min was used and the heating time of the constant temperature was 1 h. Because the aim of the study was to research the residual mechanical behaviors of concrete after exposure to high temperatures, the specimens should be tested after cooling down. Although the high thermal gradients (Mindeguia et al. 2010) and moisture clog (Chen et al. 2009) often occur during the process of rapid heating, little damage caused by thermal gradients and moisture clog occurred during the process of cooling. Besides, when the temperature is above 300 °C, the calcium oxide produced during heating will turn into the calcium hydroxide in the cooling process, which has the same influence on all specimens. As a result, to research the residual mechanical properties of concrete after exposure to high temperatures, the method of natural cooling is the most widely-used one that most researchers accept in their studies. After the heating process was finished, the specimens were carefully taken out and cooled to the normal temperature in nature. It should be noted that the specimens were heated to 800 °C in the preliminary test, but they were almost completely damaged when the heating was finished, just as shown in Fig. 1. Therefore, the upper limit of temperatures was set as 600 °C.

### 2.2 Nonlinear Resonance Vibration Tests

The experimental setup used for damage evaluation and the schematic diagram designed by Park et al. (2014) are shown in Fig. 2. After exposure to different temperatures, corresponding concrete specimens were taken out for the damage measurement. The accelerometer was glued onto the middle part of the specimen and connected to the DH5960 dynamic strain indicator. A spongy cushion

**Table 1 Concrete mix proportions by weight.**

Mass of concrete ingredients (kg/m <sup>3</sup> )					
Water	Cement	Fly ash	Sand	Aggregate	Water reducer
205	328	82	668	1089	2.05



**Fig. 1** The old concrete specimen was damaged when the high temperature was set as 800 °C in the preliminary test.

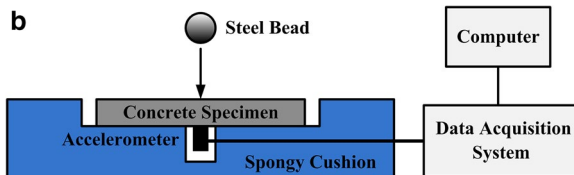


**Fig. 2** **a** The experimental setup used for damage evaluation; **b** The schematic diagram.

with a hollow part was adopted as the support system, which was used to isolate the accelerometer and keep the vibration response free. A steel bead with a diameter of 15 mm and a weight of 13.7 g was taken as a dynamic driving force. The kinetic energy was changed by dropping the steel bead onto the opposite middle part of the specimen in different heights. The frequency of sampling was adjusted to 50 kHz in the test, and two specimens were used for measuring under each temperature. For each specimen, the dropping height of the steel bead was changed for 8 times to make sure that the impact energy changed in each dropping test.

### 2.3 Mercury Intrusion Porosimetry (MIP)

It is assumed in the principle of MIP (Cook and Hover 1999) that the inside pores are cylindrical, which are connected to the outside surface of materials, and the mercury can be injected into the pores under the applied pressure  $P$ . Based on the assumption above, Washburn equation is used in the study to calculate the pore radius, which is related to the volume of mercury under the applied pressure  $P$  (Kumar and Bhattacharjee 2003b):

$$r = \frac{-4\gamma \cos \phi}{P} \quad (3)$$

where  $r$  is the pore radius corresponding to the applied pressure  $P$ ,  $\phi$  is the contact angle between mercury and pore wall (140°), and  $\gamma$  is the surface tension of mercury (0.480 N/m). The mercury can only intrude into the pores of the corresponding size under a given level of pressure, and the pore volume of the pore size is equal to that of the mercury intrusion. As the pressure is elevated, the pore size distribution of porous materials is able to be calculated by the volume of mercury. Four pieces of samples of 3–6 mm size without aggregates were cut carefully from the middle part of specimens under each temperature and dried in a furnace at 105 °C until the mass was kept constant. After MIP, the pore size analysis was carried out and two test results were averaged for the first inspection. If the difference between the two results tested at the same temperature was more than 5%, the other two samples were to be tested and the data from the bigger-error specimen should be abandoned. Finally, the pore size distribution curve was obtained at each temperature.

### 2.4 Splitting Hopkinson Pressure Bar Tests (SHPB)

Based on splitting Hopkinson pressure bar (SHPB), the impact splitting tensile strength of old concrete cores after exposure to high temperatures was measured. The schematic diagram of the SHPB setup in the study is shown in Fig. 3. The SHPB was made of the incident bar and the transmitter bar with a Brazilian disc specimen put between them. During the impact test, the incident wave was generated as the striker bar impacted the incident bar, and then the wave propagated in the incident bar until it entered the disk. At this moment, a portion of the incident wave returned back and turned into the reflected wave, while the other portion entered the transmitter bar and transformed into the transmitted wave. According to the theory of the elastic wave propagation, the stress state of the Brazilian disc could be calculated by the transformation of the above waves before failure occurred. Strain gauges were glued onto the middle of the incident bar and the transmitter bar to collect the wave

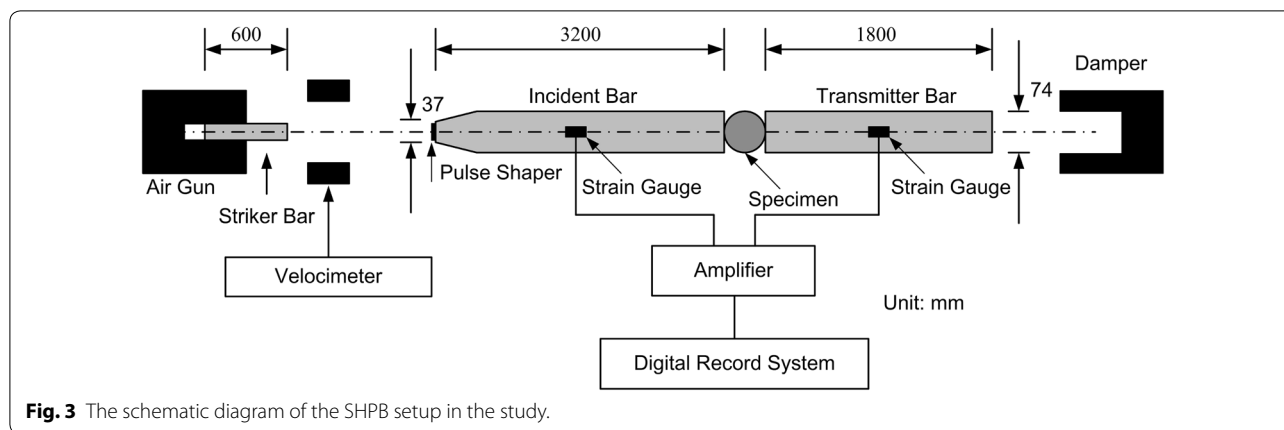


**Fig. 3** The schematic diagram of the SHPB setup in the study.

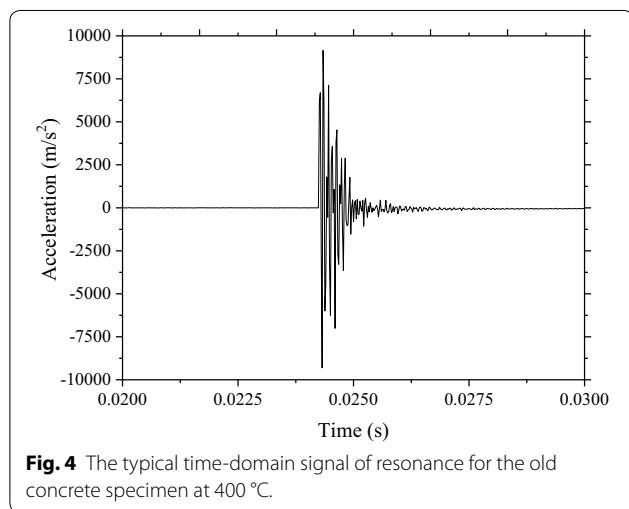


**Fig. 4** The typical time-domain signal of resonance for the old concrete specimen at 400 °C.

signals. Meanwhile, a thin copper disk was glued onto the interface of the striker bar and the incident bar for pulse-shaping. A velocimeter was used to measure the impact velocity of the striker bar, and its location is shown in Fig. 3. The data was collected by the ultra-dynamic strain amplifier and the sampling frequency was 5 MHz. The impact gas pressure in the study was adjusted to 0.3 MPa, 0.4 MPa and 0.5 MPa, and three old concrete specimens at each temperature were impacted under the same air pressure.

### 3 Damage Evaluation

#### 3.1 Nonlinear Resonance Vibration Results

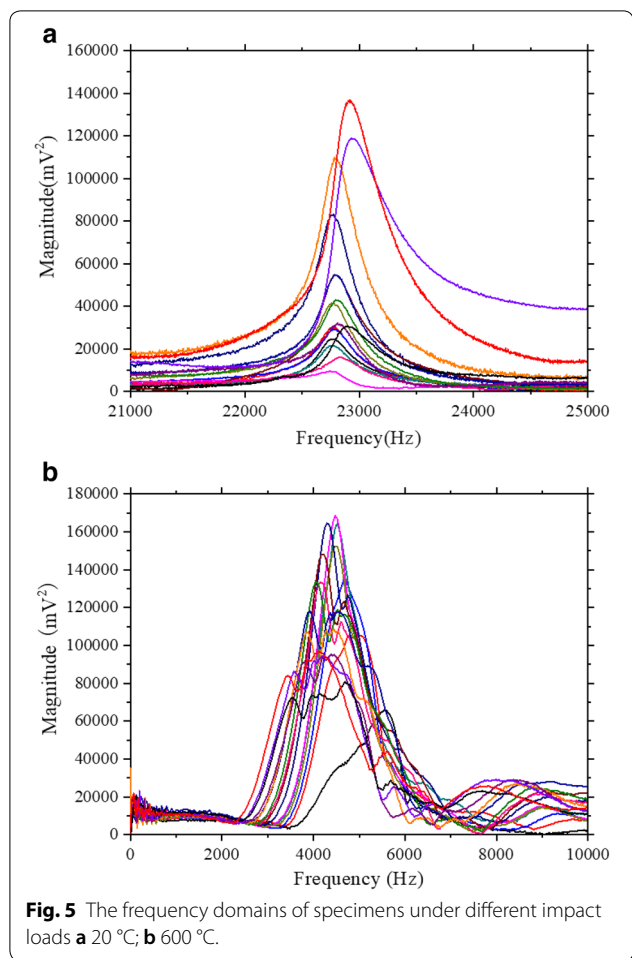
Based on the results of nonlinear resonance vibration tests, the typical time-domain signal of resonance for the old concrete cores at 400 °C is shown in Fig. 4. It can be seen that the values of acceleration collected by the accelerometer decrease with the increase of time. Fast-Fourier transform (FFT) is used to convert the time-domain signal into the frequency domain. With the variation of

dropping heights of the steel bead, the peak acceleration and the peak resonance frequency in the middle part of the specimen change at the same time, which shows obvious nonlinear resonance characteristics. Figure 5a, b show the frequency domains of specimens at 20 °C and 600 °C under different impact loads. It is shown in Fig. 5a that the peak resonance frequency fluctuates in a small range under different impact loads, except for the relatively large fluctuation of some particular data. According to the study done by Abeele and Carmeliet (2000), the peak resonance frequency varies slightly with the change of amplitude when the material is undamaged. As the damage becomes more severe, the variation of peak resonance frequency becomes more obvious. Therefore, the results shown in Fig. 5a may be explained by the inevitable damage caused by the porous and heterogeneous properties of old concrete. From Fig. 5b, it can be found that the variation range of peak resonance frequency is larger than that shown in Fig. 5a, which shows the fact that high temperatures can make the damage of concrete become more severe.

In order to describe the nonlinear resonance characteristics, the equation proposed by Abeele et al. (2001) is used to describe the relationship between the strain amplitude and the relative resonance frequency:

$$\frac{f_0 - f}{f_0} = \alpha_h \Delta \varepsilon \tag{4}$$

where  $f_0$  is the linear resonance frequency,  $f$  is the measured nonlinear resonance frequency related to the resonance amplitude,  $\alpha_h$  is the hysteretic nonlinearity parameter, and  $\Delta \varepsilon$  is the strain amplitude. The strain amplitude here indicates the variation of strain caused by impact loads, therefore the values of strain amplitude are directly proportional to the peak accelerations (Abeele and Carmeliet 2000; Leśnicki et al. 2011). As a result, Eq. (4) can be rewritten as:



$$\frac{f_0 - f}{f_0} = \beta_h a_{max} \tag{5}$$

where  $\beta_h$  is the hysteretic nonlinearity parameter proportional to  $\alpha_h$ ,  $a_{max}$  is the peak acceleration in the time domain. Because the linear resonance frequency  $f_0$  has no relevance to the resonance amplitude, the value is hard to be directly obtained by tests. As a result, in the paper, linear regression is used to calculate the value of the linear resonance frequency  $f_0$ . Figure 6 shows the relation between the nonlinear resonance frequencies and the peak accelerations of old concrete cores at 600 °C. The linear resonance frequency  $f_0$  is the value of the intercept of the ordinate by the linear regression. After the calculation, Table 2 shows the linear resonance frequency of old concrete cores after exposure to different high temperatures. It can be seen from Table 2 that the linear resonance frequencies of old concrete cores after exposure to 200 °C and those at the normal temperature have little difference, and when the heating temperature rises, the

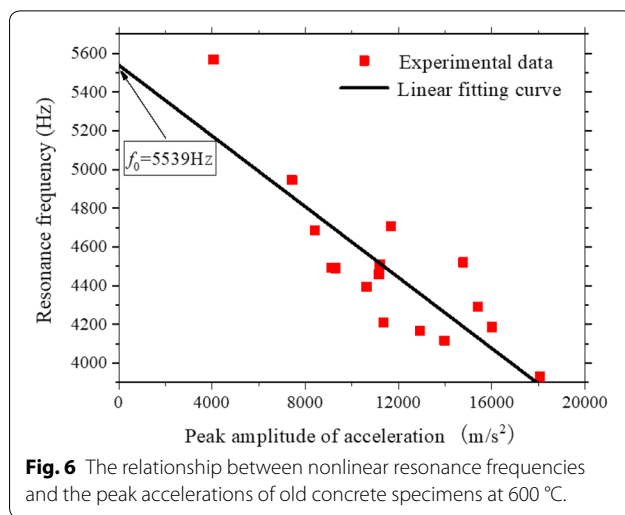
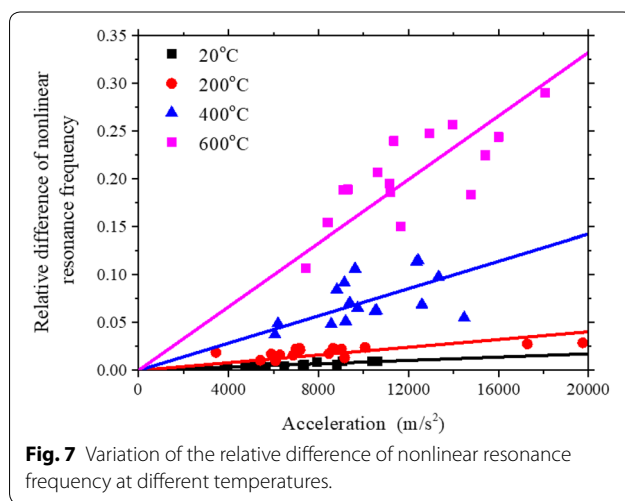


**Table 2** Linear resonance frequency ( $f_0$ ) of concrete with different damage degrees.

T (°C)	20 °C	200 °C	400 °C	600 °C
$f_0$ (Hz)	23,502	23,491	11,689	5539



damage of old concrete cores becomes larger while the linear resonance frequency decreases.

The variation of nonlinear resonance frequencies of concrete specimens after exposure to different high temperatures is shown in Fig. 7. It can be observed from Fig. 7 that the relative difference of resonance frequencies becomes larger with the increase of peak accelerations.

The value of hysteretic nonlinearity parameter  $\beta_h$  under different high temperatures can be calculated by Eq. (5). The hysteretic nonlinearity parameter  $\beta_h$  obtained in the

experiment changes greatly with the variation of temperatures. The relationship between hysteretic nonlinearity parameters and temperatures can be obtained by regression analysis:

$$T = 5.896 \times 10^5 \times (\beta_h)^{0.623}. \tag{6}$$

The correlation coefficient of fitting curve is 0.95.

### 3.2 Discussion for Damage Estimation

In the study,  $D$  represents damage mainly influenced by temperature. When the initial damage of old concrete materials is neglected, the damage  $D$  can be expressed by Eq. (7) (Park et al. 2014):

$$D = 1 - \frac{\beta_h(20^\circ\text{C})}{\beta_h(T)} \tag{7}$$

where  $\beta_h(20^\circ\text{C})$  represents the hysteretic nonlinearity parameter at normal temperature,  $\beta_h(T)$  represents the hysteretic nonlinearity parameter at temperature  $T$ . When the temperature is  $20^\circ\text{C}$ , the specimens are not pre-damaged and the value of damage is 0. As the temperature rises, the damage becomes larger. When the damage becomes 1, the concrete specimen loses its loading capacity. The hysteretic nonlinearity parameter  $\beta_h$  and the calculated damage  $D$  in the test are shown in Table 3. To compare the test results with that of other researchers, the damage in other studies is calculated by the following equation based on the results of initial modulus obtained from other researchers:

$$D = (E_o - E_T)/E_o \tag{8}$$

where  $E_o$  represents the elastic modulus of concrete at normal temperatures,  $E_T$  represents the elastic modulus of concrete at temperature  $T$ . Figure 8 shows the comparison of damage obtained from the test and those from other researchers. From Fig. 8, it can be seen that the damage calculated from the test is a bit larger than that from Chang et al. (2006) but quite similar with that calculated from the EN 1992-1-2 (Eurocode 2004). As a result,  $D$  calculated from the nonlinear resonance can be used as the degree of damage after exposure to different temperatures.

**Table 3** The hysteretic nonlinearity parameter  $\beta_h$  ( $\times 10^{-7}$ ) and the calculated damage  $D$  of samples at different temperatures.

$T$ (°C)	20 °C	200 °C	400 °C	600 °C
$\beta_h$	8.71	20.23	71.37	166.29
$D$	0	0.57	0.88	0.95

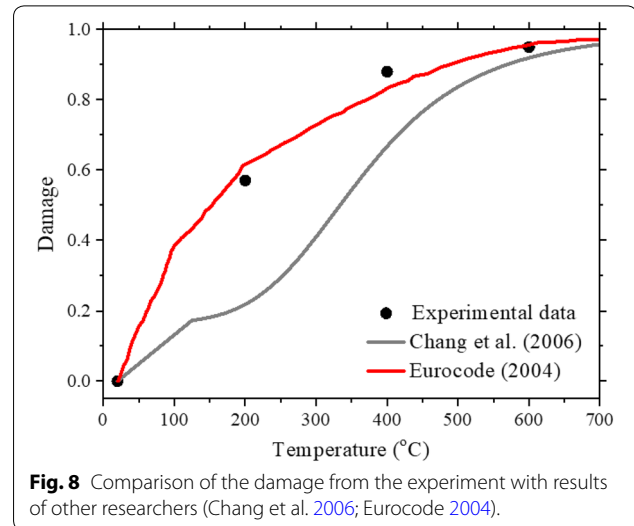


**Fig. 8** Comparison of the damage from the experiment with results of other researchers (Chang et al. 2006; Eurocode 2004).

## 4 Porosity and Pore Size Distribution

### 4.1 Mercury Intrusion Results

The porosity is the ratio between the total pore volume and the sample volume. In the MIP, the total pore volume is equal to that of the cumulative volume of mercury. Table 4 shows the average porosity of old concrete samples after exposure to different temperature. From the table, it can be indicated that the porosity obtained by MIP increases as the temperature rises. The reason may be explained that the free water evaporates and the crystal water decreases inside the concrete as the temperature goes up to  $200^\circ\text{C}$ . At the same time, C–S–H begins to break down (Piasta et al. 1984). According to the studies by Han and Choi (2011), at  $200^\circ\text{C}$ , the increase of the pore volumes is caused by the dehydration of some of the primary hydration products. Hertz (2003) stated that the pores of the material are as a rough model considered to be either open or closed. When the temperature rises, the pressure increases in the closed pores, thus the pressure difference over the separating walls between open and closed pores causes a breakdown of some of the walls. The water evaporation (Rostasy et al. 1980), moisture clog (Chen et al. 2009) and hydrating reaction (Piasta et al. 1984) finally result in the expansion of pore structures and the development of microcracks, which

**Table 4** Porosity of concrete ( $p$ ) with different temperatures.

$T$ (°C)	$p$ (%)
20	13.96
200	15.77
400	19.17
600	20.22

make the porosity become larger after exposure to higher temperatures.

Pore size distribution is the ratio between the pore volumes of different sizes and the total pore volumes. Figure 9a shows the cumulative probability curve obtained by MIP. In general, the actual pore size ranges from 50 to 225 nm. As the temperature rises, the pore size distribution curve goes up, and the average pore radius increases.

In order to better describe the influence of high temperature on the pore size distribution, the measured pore size distribution can be classified into three parts, which are mesopores (5–50 nm), middle capillary pores (50–100 nm) and larger capillary pores (> 100 nm) (Zeng et al. 2012). The pore size classification is presented in Fig. 9b.

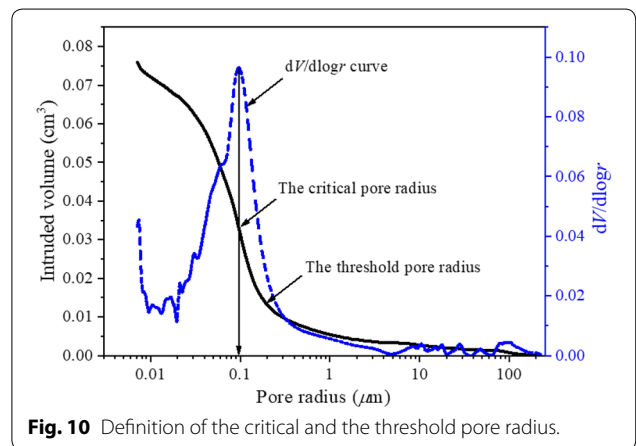
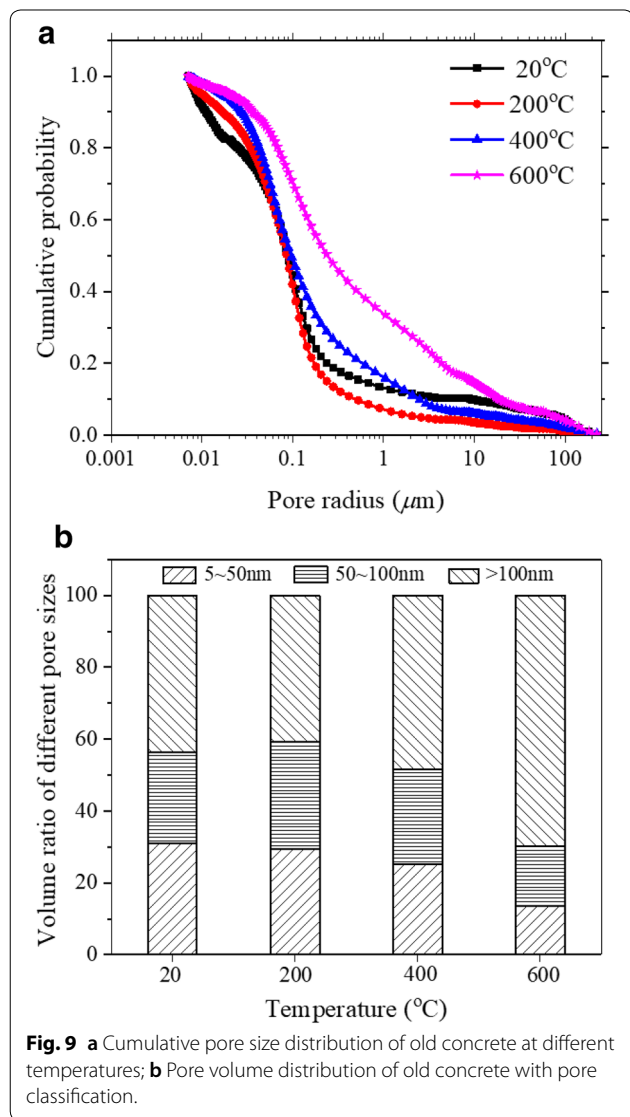
It can be seen that the volume ratio of larger capillary pores is 43.22% at normal temperature. When the temperature reaches 200 °C, the volume ratio of larger

capillary pores decreases, while the volume ratios of mesopores and middle capillary pores increase. As 600 °C is reached, the volume ratio of larger capillary pores rises to 69.83%, and the increase rate of larger capillary pores becomes higher. Meanwhile, the volume ratios of mesopores and middle capillary pores decrease and the decrease rate becomes faster. To be specific, the total volume ratio of mesopores and middle capillary pores is 56.37% at normal temperature, and decreases to 56.78% at 400 °C. When the temperature reaches 600 °C, the value continues to decrease to 30.17%, which is 26.61% smaller than that at normal temperature. The reason may be expounded as follows: besides the decomposition of hydration products and temperature stress explained above, hydrated calcium silicate continues to decompose at 600 °C, which causes further damage to hydration products. Simultaneously, mesopores and middle capillary pores feed through to each other and the micro structures of old concrete become looser as microcracks continue to develop.

The static loading–unloading curves for two different aggregates pervious concrete are drawn in Fig. 10. According to the experimental data, the EPF model was modified to obtain the relationship between the fracture parameter  $K$ , the plastic strain  $\epsilon_p$  and the unloading strain  $\epsilon_{max}$ . The initial elastic modulus and peak strain of the two aggregates pervious concrete are shown in Table 5.

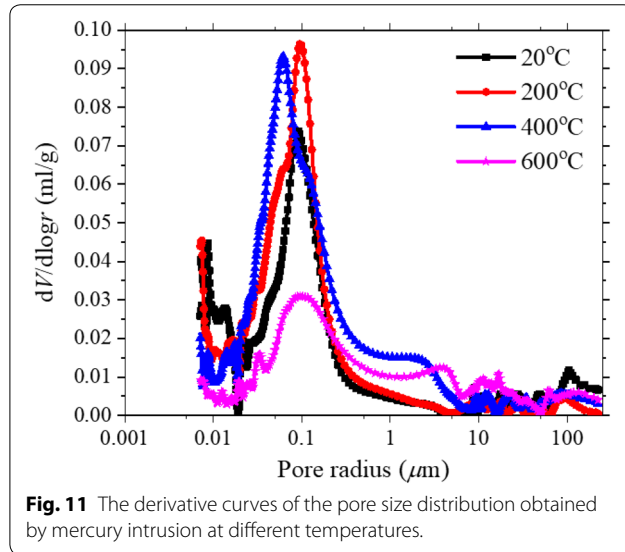
### 4.2 Critical and Threshold Pore Radius

The definitions of the critical pore radius and the threshold pore radius are shown in Fig. 10. The critical pore radius ( $r_c$ ) corresponds to the point when the maximal value of the derivative of the pore size distribution curve  $dV/d\log r$  is reached, while the threshold pore radius ( $r_t$ ) is determined by the point where mercury starts to percolate the pore system in appreciable quantity (Quenard et al. 1998). It should be noted that two peak values may



**Table 5** The critical pore radius ( $r_c$ ) and the threshold pore radius ( $r_t$ ) of concrete under different temperatures.

$T$ (°C)	$r_c$ (nm)	$r_t$ (nm)
20	89	181
200	97	200
400	99	214
600	104	330

**Fig. 11** The derivative curves of the pore size distribution obtained by mercury intrusion at different temperatures.

occur in the pore size distribution curve, but one peak value is not in the range of measurement because of the limitation of the equipment. As a result, only one peak value is obtained in the test.

The derivative curves of the pore size distribution obtained by mercury intrusion at different temperatures are shown in Fig. 11, and the corresponding critical and threshold pore radii are presented in Table 5. Experimental results show that the critical pore radius varies from 89 to 104 nm while the threshold pore radius varies from 181 to 330 nm as the temperature changes from 20 to 600 °C. Meanwhile, both values above are proportional to temperatures and the increase rate of them becomes higher. The reason may be expounded that crystal water in cement begins to evaporate and the critical and threshold pore radii begin to increase due to the decomposition of hydration products and the temperature stress when the temperature reaches 200 °C. As the temperature reaches 400 °C, the evaporation of crystal water is almost finished, hydration products continue to decompose and microcracks begin to propagate. When 600 °C is reached, hydrated calcium silicate continues to decompose and the increase rate of microcracks gets higher, therefore

the critical and threshold pore radii have a comparatively large growth.

### 4.3 Pore Fractal Dimension

The fractal theory is a method of studying complex nonlinear system. According to the conventional research method, complex research objects are often simplified into ideal models by means of assumption or abstraction, but the simplifications are bound to cause the error between the result of the study and the fact. To avoid the errors caused by simplification, the fractal theory is used in the study. The fractal theory, whose research object is the complex nonlinear system, explores the inherent law of materials. Measure and dimension are two basic mathematical parameters of the fractal theory respectively. Measure determines the set size while fractal dimension describes the heterogeneity and complicity of the system investigated.

In the pore size distribution study of materials, many mathematical models of the fractal dimension based on the MIP method have been proposed. Xu (2004) compared and summarized several methods of calculating the parameter. In the study, the mathematical model proposed by Ji et al. (1997) was used and the fractal dimension obtained from MIP was calculated by graphical analysis.

The mathematical model in the study is Menger sponge geometry model. In the model, a small cube with a side length of  $R$  is regarded as the initial element. Then the cube is divided into  $m^3$  cubes and  $n$  of them are filled with the solid phase, and  $m^3 - n$  cubes are remained. During the calculation, the process is repeated until the infinite, where the size of cubes becomes smaller and smaller, while the number of them increases continuously. The phenomenon above is similar to the evolution of pore structures, and fractal dimensions are produced during the process. The size  $r$  of the small cubes is shown as follows after the  $k$ th operation:

$$r = \frac{R}{m^k} \quad (9)$$

$$k = \frac{\log(R/r)}{\log m} \quad (10)$$

The number  $N_k$  of the remaining small cubes is shown in Eq. (11):

$$N_k = (m^3 - n)^k = (r_k/R)^{-\log(m^3 - n)/\log m} \quad (11)$$

where  $V_k$  represents the relative remaining volume of pores inside old concrete, which is calculated by the volume of intruded mercury from the large-to-small scale

sequence. The relationship between the relative remaining volume of pores and fractal dimensions can be established as follows:

$$V_k = \left(\frac{r}{R}\right)^{3-D} \tag{12}$$

Equation (13) can also be expressed as follows:

$$\log(V_k) \propto (3 - D) \log(r) \tag{13}$$

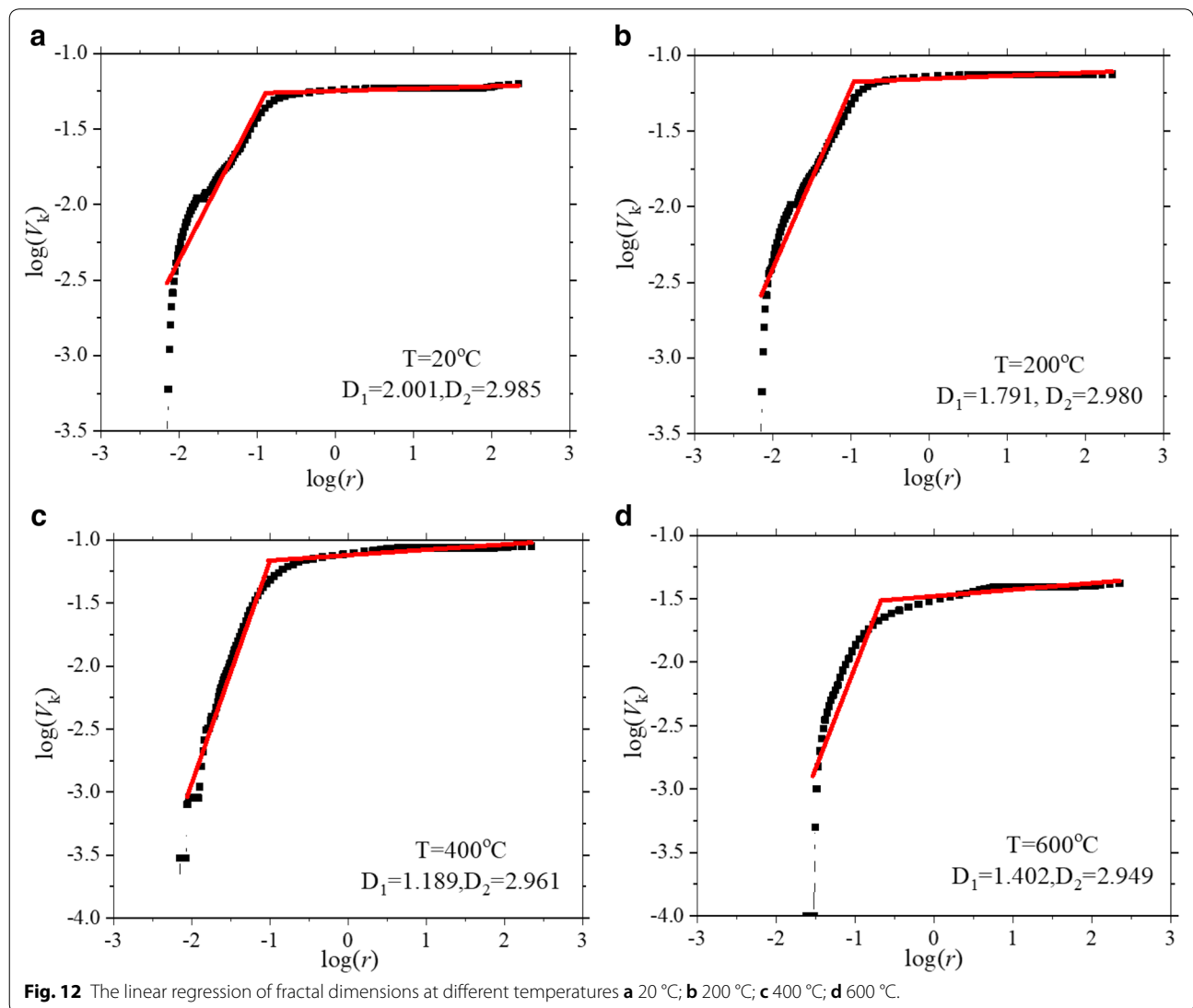
The fractal dimension can be obtained from the slope of the  $\log(V_k)$ - $\log r$  curve. The results of data analysis based on the model above are shown in Fig. 12.

It can be indicated from Fig. 12 that pore structures have the characteristic of multi-fractal on account of various formation mechanisms of them. The curves in

Fig. 12 can be divided into two parts and be fitted by linear regression. The pores inside concrete specimens can also be divided into two parts by regarding the pore radius of around 50 nm as the critical point: mesopores (<50 nm) and larger pores (>50 nm). The result is in accordance with that obtained by Xu (2004), which shows that the two groups of the pore radii above both have their fractal characteristic.

#### 4.4 Compound Lognormal Distribution

When function  $y=\ln x$  is normally distributed with mean  $\mu$  and standard  $\sigma$ , the variable  $x$  meets the lognormal distribution, whose probability density function is as follows:



$$p(x) = \frac{1}{\sqrt{2\pi\sigma^2x}} \exp \left[ -\frac{1}{2} \left( \frac{\ln(x) - \mu}{\sigma} \right)^2 \right] \quad (14)$$

where  $\mu$  and  $\sigma$  are the location parameter and the shape parameter, respectively. In calculation, several relevant parameters in a lognormal distribution are shown as follows:

$$\text{mean} = \exp(\mu + 0.5\sigma^2) \quad (15)$$

$$\text{median} = \exp(\mu) \quad (16)$$

$$\text{coefficient of variation} = \exp(\sigma^2) - 1 \quad (17)$$

$$\text{variance} = \text{mean}^2 [\exp(\sigma^2) - 1]. \quad (18)$$

The probability density function of the model can be defined as follows:

$$p(x) = f_1p(x, \mu_1, \sigma_1) + f_2p(x, \mu_2, \sigma_2) + f_3p(x, \mu_3, \sigma_3) \quad (19)$$

$$\sum_{i=1}^3 f_i = 1 \quad (20)$$

where  $f_i$  is the weighting factor of the  $i$ th lognormal subdistribution  $p(x, \mu_i, \sigma_i)$ , and  $\mu_i$  and  $\sigma_i$  are the location parameter and the shape parameter of the  $i$ th subdistribution, respectively. Studies have shown that if an attribute of a system can be described by two or more lognormal distributions, two or more phenomena are likely to occur in that system (Xu 2004).

Based on the study of pore size distribution in the paper, the compound lognormal distribution model is applied to pore radii of the three types mentioned in the pore size analysis. The different pore sizes have different formation mechanisms.  $f_1, f_2$  and  $f_3$  represent the weighting factors ( $f_1, f_2$  and  $f_3$ ) corresponding to the lognormal subdistributions of different types of pores.

In the study,  $x$  represents the pore radius, and  $P(x)$  represents the cumulative probability measured by MIP. Graphical analysis is often used to analyze the type of distribution model and to get the initial values of parameters in the applied model. With  $\ln x$  as the ordinate, the quantiles of normal distribution  $(\ln x - \mu)/\sigma$  as the abscissa, the curve of  $\ln x$  vs. the quantiles can be plotted. If the curve is linear in shape, then  $x$  obeys a single logarithmic distribution.

Figure 13 shows the curve of  $\ln x$  vs. the quantiles calculated from the data of MIP at 400 °C. The curve consists of three linear parts, as a result,  $x$  obeys a compound logarithmic distribution and the slope and intercept of

each segment are the location parameter  $\mu_i$  and the shape parameter  $\sigma_i$  of each part, respectively. The weighting factor corresponding to the lognormal subdistribution can be obtained by the intersection of two segments. For instance, in Fig. 13, the abscissa of the intersection of the first and second segment is located at 0.21, which corresponds to cumulative probability of 0.58. Therefore,  $f_1 = 0.58$ .

The parameters of old concrete at different temperatures are calculated and put into Table 6. It can be found in Table 6 that  $f_3$  decreases continuously as the temperature rises. The phenomenon indicates that the ratio of mesopores decreases with the increase of temperatures, which further demonstrates the previous conclusion. As the temperature rises from 20 to 200 °C, the ratio of middle capillary pores becomes larger while  $f_3$  decreases rapidly, which can be explained by the fact that part of mesopores turn into middle capillary pores in the temperature variation range. When the temperature is located in the range of 400–600 °C,  $f_1$  is on the tendency of becoming larger while  $f_2$  and  $f_3$  decrease, which indicates that the pore size tends to become larger and corresponds to the experimental results in the range of temperature variation.

Substituting the parameters into the compound lognormal distribution model, the cumulative probability values of old concrete can be predicted at each temperature. Figure 14 shows the comparison between the experimental data and calculated values of the pore size distribution at different temperatures. It can be seen from the figure that the calculated curves correspond well with the experimental curves, which illustrates the applicability of the model.

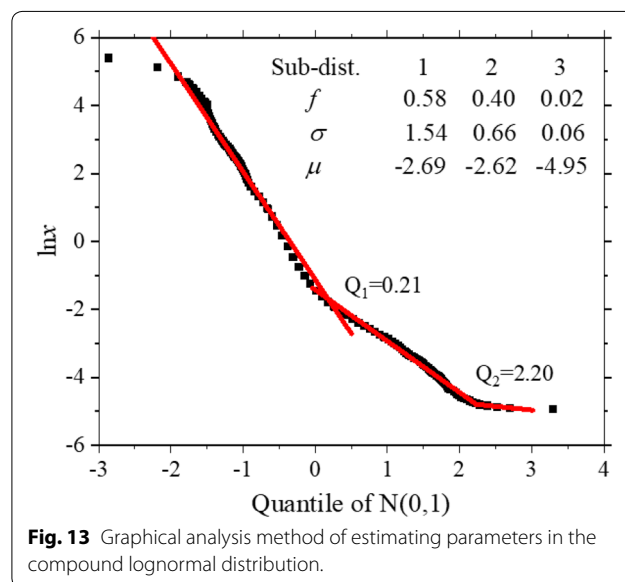


Fig. 13 Graphical analysis method of estimating parameters in the compound lognormal distribution.

**Table 6** Parameters of the compound lognormal distribution model.

$T$ (°C)	$f_1$	$\sigma_1$	$\mu_1$	$f_2$	$\sigma_2$	$\mu_2$	$f_3$	$\sigma_3$	$\mu_3$
20	0.32	2.02	-3.69	0.62	0.65	-3.86	0.06	0.07	-4.95
200	0.15	1.97	-4.58	0.82	0.52	-4.08	0.03	0.07	-4.75
400	0.29	1.78	-3.71	0.69	0.46	-3.38	0.02	0.19	-4.61
600	0.58	1.54	-2.69	0.40	0.66	-2.62	0.02	0.02	-4.95

$\chi^2$  goodness-of-fit technique can be used to compare the test results of old concrete at different temperatures with the results from the fitted distributions. The  $\chi^2$  test

is an important indice which can estimate whether the fitting data is goodness-of-fit. The goodness-of-fit technique is shown as follows:

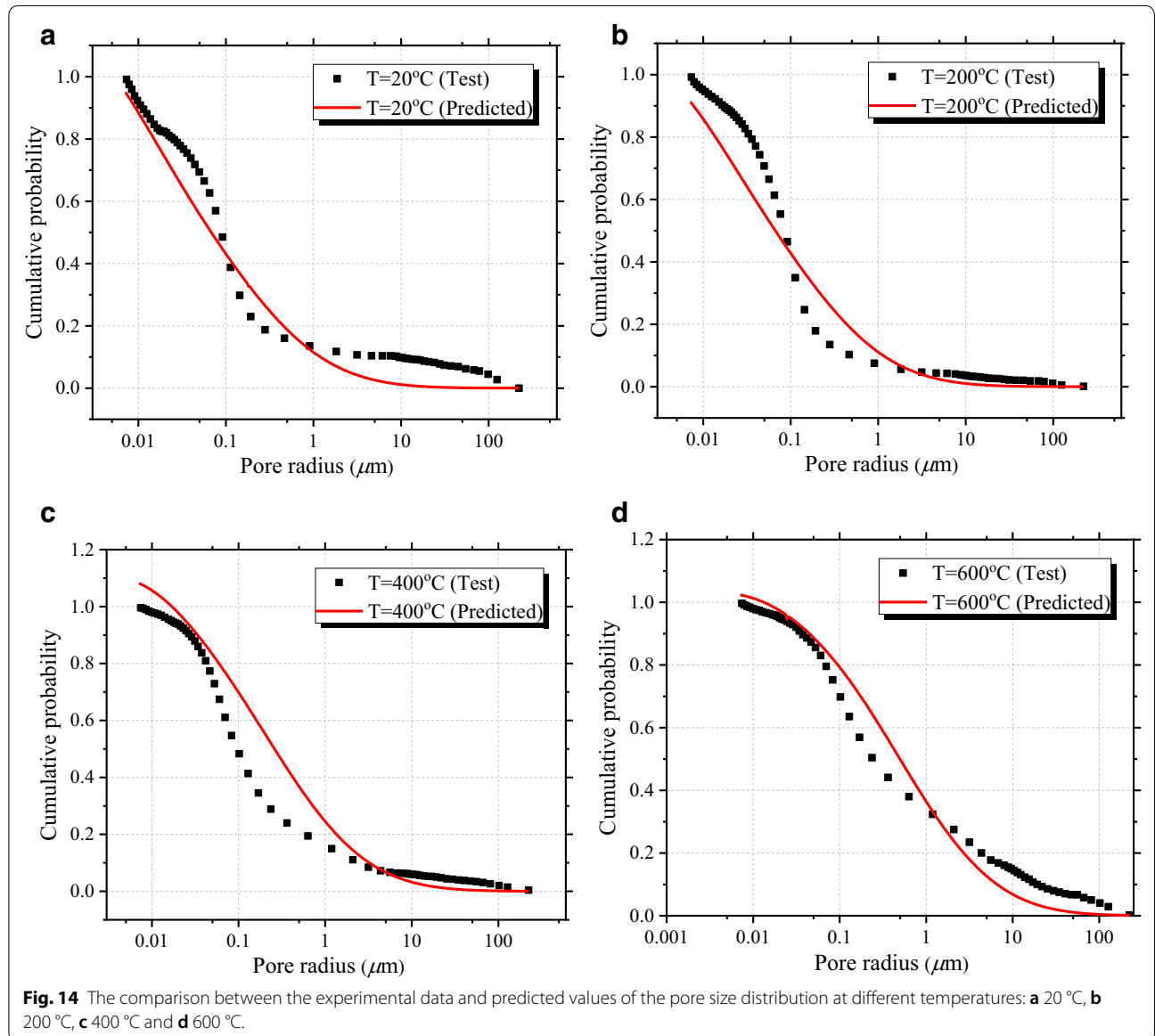


**Fig. 14** The comparison between the experimental data and predicted values of the pore size distribution at different temperatures: **a** 20 °C, **b** 200 °C, **c** 400 °C and **d** 600 °C.

$$\chi_0^2 = \sum_{i=1}^k \frac{(O_i - E_i)^2}{E_i} \tag{21}$$

where  $\chi_0^2$  is the test statistic,  $k$  is the number of bins,  $O_i$  and  $E_i$  are the observed and expected frequency in the  $i$ th interval. Besides, the sum of the observed frequency is defined as  $N = O_1 + O_2 + O_3$ , and  $E_i = NP_i$  where is the cumulative probability in the  $i$ th interval. By varying the estimated parameters of distribution until the test statistic is minimized, fits can be obtained. Then, the test statistic is compared with the critical value of  $\chi_{\alpha, k-\beta-1}^2$  with  $k-\beta-1$  degrees of freedom, where  $\beta$  is the number of estimated parameters of the distribution and  $\alpha$ -error is taken as 0.05. The hypothesis is that the pore size data followed the tested distribution should be rejected if  $\chi_0^2 > \chi_{\alpha, k-\beta-1}^2$ .

The comparison between the experimental result and the model simulation of cumulative pore size distribution is shown in Table 7. It is indicated that the correlation coefficients are close to 1 and the inequality  $\chi_0^2 < \chi_{\alpha, k-\beta-1}^2$  is met in all cases. Therefore, the compound lognormal distribution is suitable for predicting the cumulative pore size distribution curve at different temperatures.

#### 4.5 Discussion of Pore Parameters

Table 8 shows the parameters obtained from the pore size analysis of old concrete cores and the damage measured in the nonlinear resonance vibration test. As the temperature rises, expect  $D_1$  at 400 °C, the fractal dimensions in mesopores and larger pores decrease, which indicates that the correlation exists between the fractal dimension and damage. When the temperature is in the range of

**Table 7 Inspection of the compound lognormal distribution model.**

$T$ (°C)	$R^2$	$\chi_0^2$	$\chi_{\alpha, k-\beta-1}^2$
20	0.991	102.64	653.91
200	0.989	114.52	653.91
400	0.983	156.93	666.47
600	0.992	242.45	666.47

**Table 8 Parameters of old concrete at different temperatures.**

$T$ (°C)	$D_1$	$D_2$	$p$ (%)	$r_c$ (nm)	$r_t$ (nm)	$D$
20	2.001	2.985	13.96	89	181	0
200	1.791	2.980	15.77	97	200	0.57
400	1.189	2.961	19.17	99	214	0.88
600	1.402	2.949	20.22	104	330	0.95

20–400 °C, both  $D_1$  and  $D_2$  have a tendency of decrease, which can be explained that the distribution of both mesopore and larger pores are more focused in the temperature range. When the temperature varies from 400 to 600 °C, the fractal dimension of mesopores increases, while that of larger pores has little changes. The result shows that more mesopores are produced and the distribution of them is scattered. The reason for the above phenomenon may be that the hydration products continue to break down, which results in more emergences of mesopores. Moreover, the mesopores are connected to each other, which results in the emergence and centralization of larger pores. As the temperature rises, the total porosity, the critical pore radius, and the threshold pore radius increase with the accumulation of damage. Here, the correlation between the total porosity and the measured damage is fitted by power function. The result is shown as follows:

$$D = 0.446(p - p_0)^{0.411} \tag{22}$$

where  $D$  is damage,  $p$  is the total porosity after exposure to high temperatures, and  $p_0$  is the total porosity at normal temperature, whose value is 13.96% in the test. The correlation coefficient  $R^2$  is equal to 0.99.

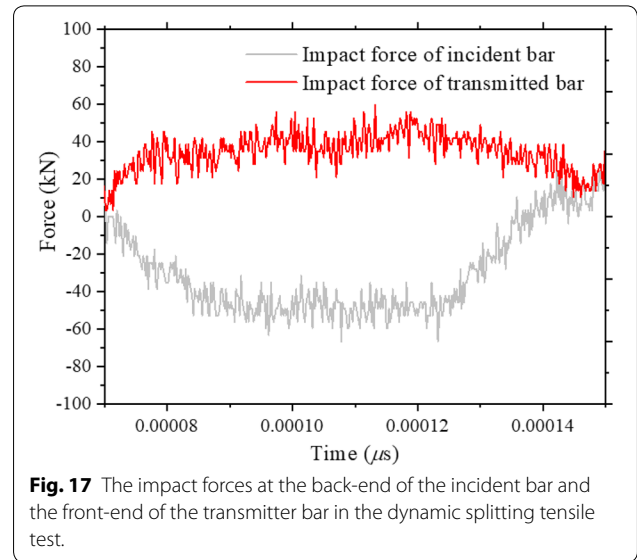
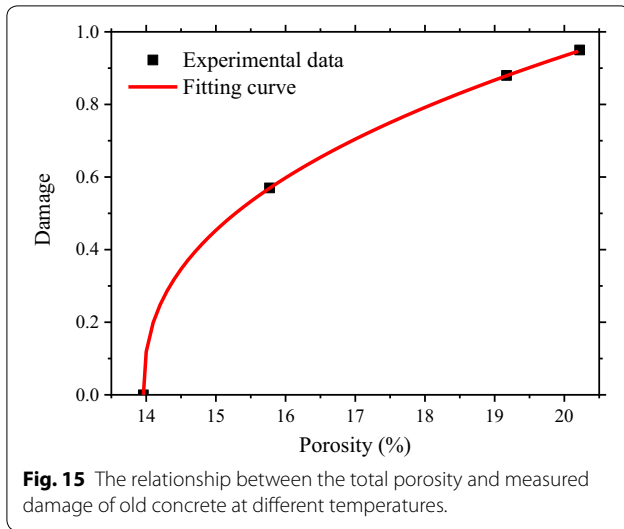
The predicted result is shown in Fig. 15. The fitting result is in correspondence with the test results. It should be noted that the temperatures adopted in the test are limited, which results in the phenomenon that the correlation coefficient is very close to 1. For further study, more temperature conditions should be considered to further improve the accuracy of test results.

#### 5 Impact Splitting Tensile Behavior

During the impact process, the forces of the back-end of the incident bar and the front-end of the transmitter bar can be expressed by Eq. (23) (Chen et al. 2014):

$$\begin{cases} P_1(t) = S_B E (\varepsilon_i(t) + \varepsilon_t(t)) \\ P_2(t) = S_B E \varepsilon_t(t) \end{cases} \tag{23}$$

where  $P_1(t)$  is the impact force on the back-end of the incident bar,  $P_2(t)$  is the impact force on the front-end of the transmitter bar,  $S_B$  is the sectional area of the incident bar and the transmitter bar, whose value is 0.0043 m<sup>2</sup> in the study, and  $E$  is the elastic modulus of the bar, whose



value is 210 GPa in the study.  $\varepsilon_i(t)$ ,  $\varepsilon_r(t)$  and  $\varepsilon_t(t)$  are the incident strain, the reflected strain and the transmitted strain obtained by the strain gauges. According to the experimental results, the experimental signals obtained by the strain gauges are shown in Fig. 16.

According to Eq. (23), the impact forces on the back-end of the incident bar and the front-end of the transmitter bar can be calculated, as shown in Fig. 17. It can be found that the impact forces on the back-end of the incident bar and the front-end of the transmitter bar are equivalent within the range of permitted errors. On the basis of the Newton third law, the forces at both ends of the tested specimen are equivalent and the specimen can be regarded within equilibrium. As a result, based upon the hypothesis above, the forces at both ends of the specimen can be regarded proportional to the transmitted stress (Lok et al. 2003). The central stress of the old

concrete specimen can be calculated by the static splitting tensile equation (Chen et al. 2014; Wang et al. 2004):

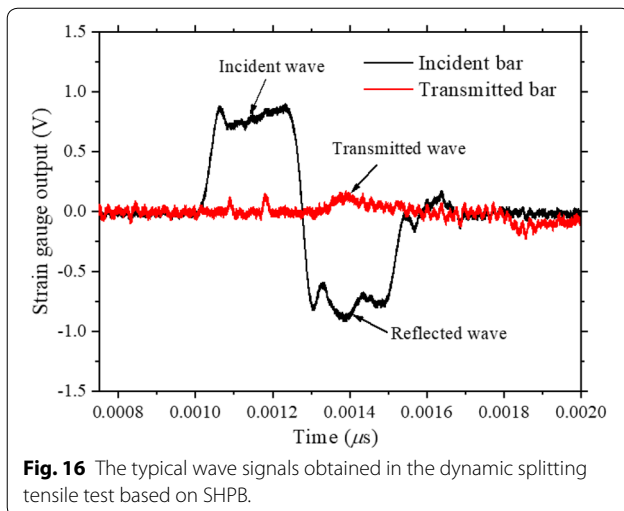
$$\sigma_t = \frac{P_{2max}}{\pi DL} Y(\alpha) \tag{24}$$

where  $\sigma_t$  is the maximal tensile stress at the center of old concrete specimen,  $P_{2max}$  is the maximal impact force on the front-end of the transmitter bar during the impact process,  $D$  is the specimen diameter,  $L$  is the specimen length, and  $Y(\alpha)$  is the non-dimensional stress which is related to the loading angle  $\alpha$ . In the case of the study, the value of  $\alpha$  is  $0^\circ$ , and the corresponding  $Y$  equals to 1.

The dynamic splitting tensile strengths of old concrete specimens can be calculated under different impact velocities. The average results of calculation are shown in Fig. 18. Obviously, the dynamic splitting tensile strengths of old concrete cores decrease significantly with the increase of temperatures under the same gas pressures. Meanwhile, under the same temperature, with the increase of the gas pressures and the impact velocities, the dynamic strengths of old concrete increase, and the reason for the above phenomenon can be explained as strain rate effect (Chen et al. 2014, 2015, 2016).

Studies have shown that there exists a close correlation between the total porosity and the strength of concrete materials (Chen et al. 2013; Zhang 1998). Commonly the strength of concrete decreases with the increase of the total porosity. Zhang (1998) summarized previous studies and proposed the quantitative relationship between the total porosity and the flexural tensile strength:

$$f_{cr} = f_{cr0}(1 - p)^k \tag{25}$$



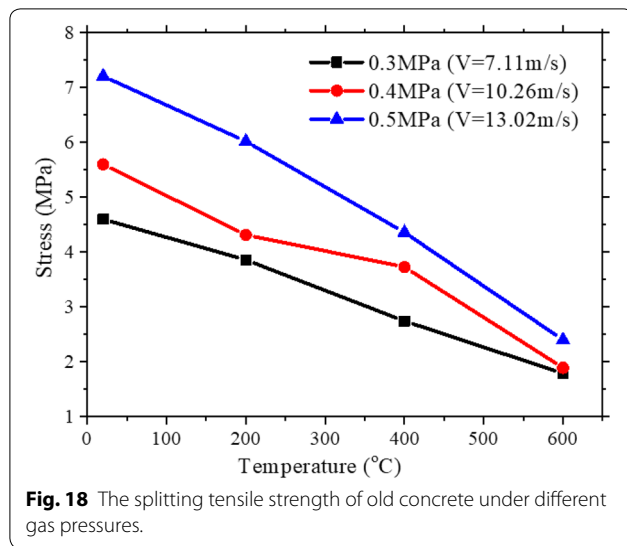


**Table 9** Parameter  $b$  at different gas pressures.

$P_g$ (MPa)	Velocity (m/s)	$b$	$R^2$
0.3	7.11	0.272	0.98
0.4	10.26	0.280	0.90
0.5	13.02	0.290	0.95

where  $f_{cr}$  is the flexural tensile strength when the concrete is damaged,  $f_{cr0}$  is the flexural tensile strength of concrete as the idealized porosity is 0,  $p$  is the total porosity, and  $k$  is the material parameter. Based on Eqs. (22), (25) can be modified into Eq. (26):

$$f_{ts,T}(P_g) = f_{ts,20}(P_g)(1 - D)^b \quad (26)$$

where  $f_{ts,T}(\dot{\epsilon})$  is the dynamic splitting tensile strength after the concrete is exposed to high temperatures,  $f_{ts,20}(\dot{\epsilon})$  is the dynamic splitting tensile strength at normal temperature,  $P_g$  is the gas pressure,  $D$  is the damage degree, which is measured by nonlinear resonance vibration, and  $b$  is the material parameter. Parameter  $b$  at different gas pressures is shown in Table 9 by the fitting method. The predicted results fit well with the test results, and the value of  $b$  increase slightly with the increase of gas pressure, as shown in Table 9. The average value of  $b$  is 0.281.

## 6 Discussion

The damage evolution and strength degradation are found to be nonlinear in the study. As the temperature goes higher, more damage accumulates in concrete and the strength decreases. When the temperature approaches 600 °C, the porosity increases largely and

the dynamic strength only remains 30% of that at normal temperature, which is unqualified for structures such nuclear power station and rocket station. To improve fire resistance, polypropylene fibers (Zeiml et al. 2006), fly ash (Ibrahim et al. 2012) and carbonate aggregate (Kodur et al. 2003) may be used in the casting of concrete, and the above testing and calculation method can be used to evaluate the microscopic and macroscopic properties of concrete of different fire resistance. Studies on fire resistance of concrete should be performed in the future.

## 7 Conclusions

In the study, the cores of 10-year-old concrete were tested. The nonlinear resonance vibration, MIP, and SHPB technique were used for damage evaluation, pore size distribution study and impact splitting tensile test, respectively. Conclusions can mainly be drawn as follows:

Based on the theory of nonlinear resonance vibration, the nonlinear resonance frequency varied when the impact energy changed, and the degree of variation was directly related to damage. The concept of hysteretic nonlinearity parameter  $\beta_h$  was used to indicate the relative difference of the nonlinear resonance frequencies, accordingly the degree of damage was defined. In the study, the measured damages at the temperature of 20 °C, 200 °C, 400 °C and 600 °C were 0, 0.57, 0.89 and 0.95, respectively.

After exposure to different high temperatures, microscopic characteristics of old concrete, such as the total porosity, pore size distribution, the critical pore radius, the threshold pore radius and the fractal dimension, were studied on the basis of MIP. It was found that not only the total porosity but also the critical pore radius and the threshold pore radius increased with the increase of temperatures. A mathematical model was applied to studying the fractal dimensions of pore sizes, which showed that the fractal dimensions increased with the increase of temperatures expect the condition of 400 °C. Moreover, a compound lognormal distribution simulated very well the pore size distributions of old concrete at different temperatures. Finally, a power function was found suitable to be applied to the relationship between the total porosity and the damage measured by the nonlinear resonance vibration.

The dynamic splitting tensile strengths of old concrete were obtained by impact splitting tensile tests based on SHPB. The relationship between the damage measured by the nonlinear resonance vibration and the dynamic splitting tensile strengths of old concrete cores was established under different gas pressures by modifying the model proposed by Zhang. It was found that the material parameter  $b$  increased slightly with the

increase of gas pressure and the average value of  $b$  was 0.281.

#### Acknowledgements

The research is based upon the work supported by the National Natural Science Foundation of China (Grant No. 51979090); Natural Science Foundation for Excellent Young Scholars of Jiangsu Province (Grant No. BK20190075); Young Elite Scientists Sponsorship Program by China Association for Science and Technology (Grant No. 2017QNRC001).

#### Authors' contributions

XC was a major contributor in the design of the study and collection, analysis, and interpretation of data and in writing the manuscript. DS analyzed the results of the experiment and improved the writing of the manuscript. SG operated the experiment and summed up the test data. All authors read and approved the final manuscript.

#### Funding

Not applicable.

#### Availability of data and materials

The datasets used and analyzed during the current study are available from the corresponding author on reasonable request.

#### Competing interests

The authors declare that they have no competing interests.

#### Author details

<sup>1</sup> Key Laboratory of Concrete and Prestressed Concrete Structures of the Ministry of Education, School of Civil Engineering, Southeast University, Nanjing 210096, China. <sup>2</sup> College of Civil and Transportation Engineering, Hohai University, Nanjing 210024, China. <sup>3</sup> China Institute of Water Resources and Hydropower Research, Beijing 100048, China.

Received: 8 June 2019 Accepted: 14 January 2020

Published online: 27 March 2020

#### References

- Abeele, E. A. V. D., & Carmeliet, J. (2000). Nonlinear elastic wave spectroscopy (news) techniques to discern material damage, part II: Single-mode nonlinear resonance acoustic spectroscopy. *Research in Nondestructive Evaluation*, *12*(1), 31–42.
- Abeele, E. A. V. D., Johnson, P. A., & Sutin, A. (2000). Nonlinear elastic wave spectroscopy (news) techniques to discern material damage, part I: Nonlinear wave modulation spectroscopy (nwms). *Research in Nondestructive Evaluation*, *12*(1), 17–30.
- Abeele, E. A. V. D., Sutin, A., Carmeliet, J., & Johnson, P. A. (2001). Micro-damage diagnostics using nonlinear elastic wave spectroscopy (news). *NDT&E International*, *34*(4), 239–248.
- ASTM. (2004). *Standard specification for concrete aggregates*. West Conshohocken: ASTM C33.
- Bažant, Z. P., & Kaplan, M. F. (1996). *Concrete at high temperatures: Material properties and mathematical models*. London: Longman.
- Chan, Y. N., Luo, X., & Sun, W. (2000). Compressive strength and pore structure of high-performance concrete after exposure to high temperature up to 800 °C. *Cement and Concrete Research*, *30*(2), 247–251.
- Chang, Y. F., Chen, Y. H., Sheu, M. S., & Gao, G. C. (2006). Residual stress–strain relationship for concrete after exposure to high temperatures. *Cement and Concrete Research*, *36*(10), 1999–2005.
- Chen, X., Ge, L., Chen, C., & Xu, L. (2016). Influence of initial static splitting tensile loading on dynamic compressive strength of concrete cores under high strain rates. *ASCE Journal of Performance of Constructed Facilities*, *30*(6), 06016002.
- Chen, X. T., Rougelot, T., Davy, C. A., Chen, W., Agostini, F., Skoczylas, F., et al. (2009). Experimental evidence of a moisture clog effect in cement-based materials under temperature. *Cement and Concrete Research*, *39*(12), 1139–1148.
- Chen, X., Wu, S., & Zhou, J. (2013). Influence of porosity on compressive and tensile strength of cement mortar. *Construction and Building Materials*, *40*, 869–874.
- Chen, X., Wu, S., & Zhou, J. (2014). Quantification of dynamic tensile behavior of cement-based materials. *Construction and Building Materials*, *51*, 15–23.
- Chen, X., Xu, L., & Wu, S. (2015). Influence of pore structure on mechanical behavior of concrete under high strain rates. *ASCE Journal of Materials in Civil Engineering*, *28*(2), 04015110.
- Choi, W. C., Kim, S. W., Jang, S. J., & Yun, H. D. (2017). Research trends and design guidelines for fire resistance of structural concrete in South Korea. *Magazine of Concrete Research*, *69*(7), 347–364.
- Cook, R. A., & Hover, K. C. (1999). Mercury porosimetry of hardened cement pastes. *Cement and Concrete Research*, *29*(6), 933–943.
- De Bruyn, K., Bescher, E., Ramseyer, C., Hong, S., & Kang, H. K. (2017). Pore structure of calcium sulfoaluminate paste and durability of concrete in freeze–thaw environment. *International Journal of Concrete Structures and Materials*, *11*(1), 59–68.
- Eunmi, R., Yeongsoo, S., & Heesun, K. (2018). Effect of loading and beam sizes on the structural behaviors of reinforced concrete beams under and after fire. *International Journal of Concrete Structures and Materials*, *12*(1), 54–63.
- Eurocode (2004). Design of concrete structures–Part 1–2: General rules–Structure Fire Design, EN 1992-1-2, European Committee for Standardization.
- Feng, W., Liu, F., Yang, F., Li, L., & Jing, L. (2018). Experimental study on dynamic split tensile properties of rubber concrete. *Construction and Building Materials*, *165*, 675–687.
- Gao, W. Y., Dai, J. G., & Teng, J. G. (2017). Fire resistance of RC beams under design fire exposure. *Magazine of Concrete Research*, *69*(8), 402–423.
- Gonzalez-Corominas, A., Etxebarria, M., & Poon, C. S. (2016). Influence of steam curing on the pore structures and mechanical properties of fly-ash high performance concrete prepared with recycled aggregates. *Cement & Concrete Composites*, *71*, 77–84.
- Güneşyisi, E., Gesoğlu, M., & Mermerdaş, K. (2008). Improving strength, drying shrinkage, and pore structure of concrete using metakaolin. *Materials and Structures*, *41*, 937–949.
- Hager, I., Tracz, T., Śliwiński, J., & Krzemień, K. (2016). The influence of aggregate type on the physical and mechanical properties of high-performance concrete subjected to high temperature. *Fire and Materials*, *40*(5), 668–682.
- Han, M. C., & Choi, H. K. (2011). The effect on mechanical properties and micro-structure of high strength concrete at elevated temperatures. *Journal of the Architectural Institute of Korea: Structure and Construction*, *27*(3), 123–130.
- Hertz, K. D. (2003). Limits of spalling of fire-exposed concrete. *Fire Safety Journal*, *38*(2), 103–116.
- Ibrahim, R., Hamid, R., & Taha, M. (2012). Fire resistance of high-volume fly ash mortars with nanosilica addition. *Construction and Building Materials*, *36*, 779–786.
- Isojeh, B., El-Zeghayar, M., & Vecchio, F. (2017). Fatigue behavior of steel fiber concrete in direct tension. *Journal of Materials in Civil Engineering*, *29*(9), 04017130.
- Ji, X., Chan, S. Y. N., & Feng, N. (1997). Fractal model for simulating the space-filling process of cement hydrates and fractal dimensions of pore structure of cement-based materials. *Cement and Concrete Research*, *27*(11), 1691–1699.
- Kodur, V., Cheng, F., Wang, T., & Sultan, M. (2003). Effect of strength and fiber reinforcement on fire resistance of high-strength concrete columns. *Journal of Structural Engineering*, *129*(2), 253–259.
- Kumar, R., & Bhattacharjee, B. (2003a). Porosity, pore size distribution and in situ strength of concrete. *Cement and Concrete Research*, *33*(1), 155–164.
- Kumar, R., & Bhattacharjee, B. (2003b). Study on some factors affecting the results in the use of MIP method in concrete research. *Cement and Concrete Research*, *33*(3), 417–424.
- Leśnicki, K. J., Kim, J. Y., Kurtis, K. E., & Jacobs, L. J. (2011). Characterization of ASR damage in concrete using nonlinear impact resonance acoustic spectroscopy technique. *NDT and E International*, *44*(8), 721–727.
- Lok, T. S., Zhao, P. J., & Lu, G. (2003). Using the split Hopkinson pressure bar to investigate the dynamic behaviour of SFRC. *Magazine of Concrete Research*, *55*(2), 183–191.
- Mindeguia, J. C., Pimienta, P., Noumowé, A., & Kanema, M. (2010). Temperature, pore pressure and mass variation of concrete subjected to high

- temperature—Experimental and numerical discussion on spalling risk. *Cement and Concrete Research*, 40(3), 477–487.
- Monette, L., Gardner, N., & Grattanbellew, P. (2002). Residual strength of reinforced concrete beams damaged by alkali-silica reaction—Examination of damage rating index method. *ACI Materials Journal*, 99(1), 42–50.
- Park, S. J., Park, G. K., Yim, H. J., & Kwak, H. G. (2015). Evaluation of residual tensile strength of fire-damaged concrete using a non-linear resonance vibration method. *Magazine of Concrete Research*, 67(5), 235–246.
- Park, G. K., & Yim, H. J. (2017). Evaluation of fire-damaged concrete: An experimental analysis based on destructive and nondestructive methods. *International Journal of Concrete Structures and Materials*, 11(3), 447–457.
- Park, S. J., Yim, H. J., & Kwak, H. G. (2014). Nonlinear resonance vibration method to estimate the damage level on heat-exposed concrete. *Fire Safety Journal*, 69, 36–42.
- Parra, C., Valcuende, M., & Gómez, F. (2011). Splitting tensile strength and modulus of elasticity of self-compacting concrete. *Construction and Building Materials*, 25(1), 201–207.
- Pei, Y., Agostini, F., & Skoczylas, F. (2017). The effects of high temperature heating on the gas permeability and porosity of a cementitious material. *Cement and Concrete Research*, 95, 141–151.
- Piasta, J., Sawicz, Z., & Rudzinski, L. (1984). Changes in the structure of hardened cement paste due to high temperature. *Matériaux et Construction*, 17(4), 291–296.
- Quenard, D. A., Xu, K., Künzel, H. M., Bentz, D. P., & Martys, N. S. (1998). Micro-structure and transport properties of porous building materials. *Materials and Structures*, 31(5), 317–324.
- Rostasy, F. S., Weiß, R., & Wiedemann, G. (1980). Changes of pore structure of cement mortars due to temperature. *Cement and Concrete Research*, 10(2), 157–164.
- Wang, Q. Z., Jia, X. M., Kou, S. Q., Zhang, Z. X., & Lindqvist, P. A. (2004). The flattened Brazilian disc specimen used for testing elastic modulus, tensile strength and fracture toughness of brittle rocks: Analytical and numerical results. *International Journal of Rock Mechanics and Mining Sciences*, 41(2), 245–253.
- Xu, Y. (2004). Calculation of unsaturated hydraulic conductivity using a fractal model for the pore-size distribution. *Computers and Geotechnics*, 31(7), 549–557.
- Zeiml, M., Leithner, D., Lackner, R., & Mang, H. (2006). How do polypropylene fibers improve the spalling behavior of in situ concrete? *Cement and Concrete Research*, 36(5), 929–942.
- Zeng, Q., Li, K., Fen-Chong, T., & Dangla, P. (2012). Pore structure characterization of cement pastes blended with high-volume fly-ash. *Cement and Concrete Research*, 42(1), 194–204.
- Zhang, B. (1998). Relationship between pore structure and mechanical properties of ordinary concrete under bending fatigue. *Cement and Concrete Research*, 28(5), 699–711.
- Zhang, L., Yan, X., Wang, Z., & Ma, H. (2006). Experimental study on the dynamic splitting tensile behaviour of concrete. *Key Engineering Materials*, 326–328, 1543–1546.
- Zhang, M., & Li, H. (2011). Pore structure and chloride permeability of concrete containing nano-particles for pavement. *Construction and Building Materials*, 25(2), 608–616.
- Zhang, Y., Shi, Y., Zhao, Y., & Yang, J. (2017). Damage in concrete lining of an operational tunnel. *ASCE Journal of Performance of Constructed Facilities*, 31(4), 06017002.

### Publisher's Note

Springer Nature remains neutral with regard to jurisdictional claims in published maps and institutional affiliations.

Submit your manuscript to a SpringerOpen<sup>®</sup> journal and benefit from:

- Convenient online submission
- Rigorous peer review
- Open access: articles freely available online
- High visibility within the field
- Retaining the copyright to your article

---

Submit your next manuscript at ► [springeropen.com](https://www.springeropen.com)

---